



Cite as

Nano-Micro Lett.

(2021) 13:114

Received: 15 February 2021

Accepted: 22 March 2021

Published online: 27 April 2021

© The Author(s) 2021

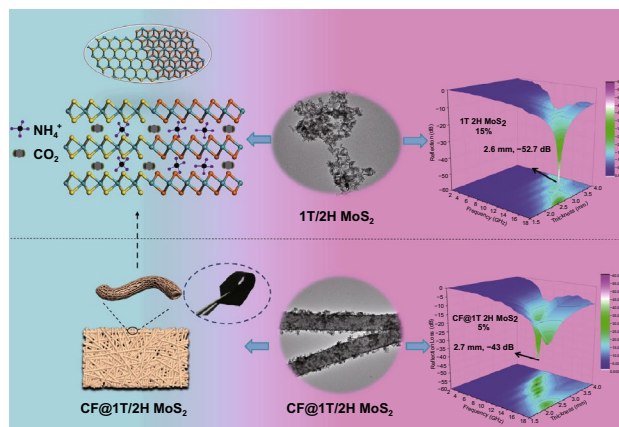
MoS₂-Decorated/Integrated Carbon Fiber: Phase Engineering Well-Regulated Microwave Absorber

Jing Yan¹, Ying Huang¹ ✉, Xiangyong Zhang², Xin Gong³, Chen Chen¹, Guangdi Nie⁴, Xudong Liu¹, Panbo Liu¹

HIGHLIGHTS

- A facile one-step hydrothermal method for producing gram-scale 1T@2H-MoS₂ by imbedding the guest molecules and ions was developed.
- The influence of different MoS₂ phase for electromagnetic absorbing properties was explored by analyzing electromagnetic parameters of 1T/2H MoS₂ and 2H MoS₂ with 50%, 40%, 30%, 20%, 15%, and 10% filler loading.
- Taking the advantage of 1T/2H MoS₂, the flexible CF@1T/2H MoS₂ was also synthesized to mind the request of flexible portable microwave absorption electronic devices.

ABSTRACT Phase engineering is an important strategy to modulate the electronic structure of molybdenum disulfide (MoS₂). MoS₂-based composites are usually used for the electromagnetic wave (EMW) absorber, but the effect of different phases on the EMW absorbing performance, such as 1T and 2H phase, is still not studied. In this work, micro-1T/2H MoS₂ is achieved via a facile one-step hydrothermal route, in which the 1T phase is induced by the intercalation of guest molecules and ions. The EMW absorption mechanism of single MoS₂ is revealed by presenting a comparative study between 1T/2H MoS₂ and 2H MoS₂. As a result, 1T/2H MoS₂ with the matrix loading of 15% exhibits excellent microwave absorption property than 2H MoS₂. Furthermore, taking the advantage of 1T/2H MoS₂, a flexible EMW absorbers that ultrathin 1T/2H MoS₂ grown on the carbon fiber also performs outstanding performance only with the matrix loading of 5%. This work offers necessary reference to improve microwave absorption performance by phase engineering and design a new type of flexible electromagnetic wave absorption material to apply for the portable microwave absorption electronic devices.



KEYWORDS Phase engineering; Electromagnetic wave absorber; 1T/2H MoS₂; 2H MoS₂; Flexible film

✉ Ying Huang, yingh@nwpu.edu.cn

¹ MOE Key Laboratory of Material Physics and Chemistry Under Extraordinary Conditions School of Chemistry and Chemical Engineering, Ministry of Education, Northwestern Polytechnical University, Xi'an 710072, People's Republic of China

² School of Materials Science and Engineering, Central South University, Changsha 410083, People's Republic of China

³ Institute of Flexible Electronics, Northwestern Polytechnical University, Xi'an 710072, People's Republic of China

⁴ Industrial Research Institute of Nonwovens and Technical Textiles, College of Textiles and Clothing, Qingdao University, Qingdao 266071, People's Republic of China



1 Introduction

With the rapid development of electronic information technology, electromagnetic wave exists everywhere in our environment that not only interferes with the electromagnetic control system and negates the effects of equipment, but also harms the physical and mental health of human beings. Therefore, it is of great significance to develop absorbing materials with electromagnetic wave absorbing ability that can both mind the requirements of “wide, thin, light and strong” [1–4]. Moreover, the miniaturization and integration of electronic circuits and components put forward the request of flexible portable microwave absorption electronic devices [5, 6].

Two-dimension (2D) materials, such as reduced graphene oxide (RGO) [7–10], MoS₂ [11–15], and new member Mxene [16–19], are usually applied as microwave absorber owing to their high specific surface area and abundant functional groups as well as defects, which will enhance the propagation paths of incident electromagnetic wave (EMW) inside absorbers by scattering effect and increase the loss through polarization relaxation loss. As one of the 2D material, MoS₂ has adjustable electrical property and can change between insulators and semiconductor metals. It has important applications in many fields such as optoelectronics [20, 21], secondary batteries [22, 23], and catalysis [24, 25]. In addition, MoS₂ also has been proved to be an effective dielectric-type EMW absorbing material. As we know, MoS₂ exists in various phase forms, such as 2H, 1T, and 3R. The natural MoS₂ usually exists in the form of 2H (hexagonal) phase that the stacking sequence is AbA, BaB (the capital and lower case letters denote chalcogen and metal atoms, respectively), showing an adjustable band gap of 1.3–1.9 eV and presenting semiconductor properties. However, the inherent low conductivity loss would limit its further practical application in microwave absorption to some extent. The octahedral coordination of 1T (triangle)-MoS₂ structure has metallic property that the stacking sequence is AbC, AbC, and belongs to metastable structure, but it shows a high electrical conductivity [26]. Therefore, combined with above advantages, the mixed phase MoS₂ (1T@2H-MoS₂) would have the great application potential in the field of microwave absorption [27].

Up to now, many researches about 2H-MoS₂ applied for EMW absorbing field have been reported [28]. Cao et al. [29] investigated the EMW absorption properties of few-layered pure MoS₂ nanosheets that prepared by a top-down exfoliation

method. The optimum electromagnetic absorbing performance parameters of MoS₂-NS/wax with 60% loading are –38.42 dB, 2.4 mm. Though the single 2H MoS₂ exhibited good EMW absorption performance, the sample in sample-paraffin needs to fill in a high proportion, this will undoubtedly limit their practical application. There already have a few advances about 1T@2H-MoS₂ as one of the components to EMW absorbing. Liu et al. [30] designed a 3D carbon foam/1T@2H-MoS₂ composites, which had the maximum reflection loss of –45.88 dB. Moreover, Che et al. [31] planted the 1T@2H-MoS₂ into RGO via ammonia insert and high-temperature annealing of 2H-MoS₂/RGO, and this composite exhibited the excellent EMW absorption ability with the sample mass ratio of 30% in sample-paraffin. These researches mainly focus on the 1T@2H-MoS₂-based composites, not involve pure 1T@2H-MoS₂, let alone profound explore the influence of different MoS₂ phase for electromagnetic absorbing properties.

In this work, we try to prepare two type phases of MoS₂ via a simple synthesis method and compare the electromagnetic parameters corresponding to different phases of MoS₂, thus obtain the excellent EMW absorber by analyzing the EMW absorbing mechanism. Normally, the transformation of MoS₂ from 2H to 1T can be achieved by chemical exfoliation or substitutional doping [32, 33], which are complex and low yield. Herein, we developed a facile one-step hydrothermal method for producing gram-scale 1T@2H-MoS₂ by imbedding the guest molecules and ions. The 2H-MoS₂ is obtained by annealing treatment of 1T@2H-MoS₂. The results show that 2H MoS₂ and 1T@2H-MoS₂ both can effectively EMW absorbing. The synergistic effect between 1T phase and 2H phase of 1T@2H-MoS₂ in EMW absorbing can further improve the dielectric loss, which makes single 1T@2H-MoS₂ has a great application prospect in the field of EMW absorbing. In addition, a flexible EMW absorbers that ultrathin 1T/2H MoS₂ grown on the carbon fiber (CF) by using the same method except the adding of CF, which performs outstanding performance only with the matrix loading of 5%, again prove the significance of this work.

2 Experimental Section

2.1 Synthesis of 1T/2H MoS₂

The (NH₄)₆Mo₇O₂₄·H₂O (0.88 g) and CH₃CSNH₂ (0.9 g) were ultrasonic dissolved in 50 mL water, and then 1.98 g

NH_4HCO_3 was added and stirred for 30 min to form a uniform liquid. The above solution was transferred into the 100-mL hydrothermal synthesis reactor and heated to 200 °C for 13 h. After cooling to room temperature, the black sediments were collected and washed with deionized water and ethanol for further use. The final product was obtained by drying in the vacuum oven for 12 h.

2.2 Synthesis of 2H MoS₂

The above 1T/2H MoS₂ was placed in an argon tube furnace and heated to 400 °C with a heating rate of 10 °C min⁻¹ for 2 h to obtain 2H MoS₂.

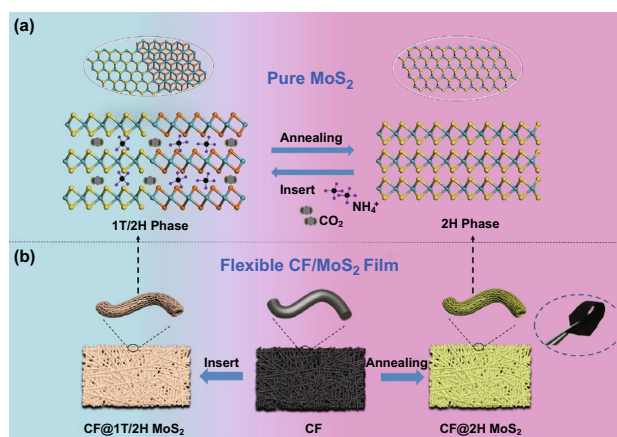
2.3 Synthesis of CF@1T/2H MoS₂ and CF@2H MoS₂

The CF is obtained via a simple electrospinning method, and the detailed process is in the supporting information [34]. The synthesis process of CF@1T/2H MoS₂ and CF@2H MoS₂ is the same as 1T/2H MoS₂ and 2H MoS₂ except adding the 0.5 g CF after the solution is transferred to hydrothermal synthesis reactor.

3 Results and Discussion

3.1 Composition and Structure

The schematic diagram of single MoS₂ is shown in Scheme 1a. The 1T/2H MoS₂ is successfully fabricated by hydrothermal method. As a guest, the ammonium bicarbonate decomposes into small molecules and ions such as NH_4^+ , H_2O , and CO_2 , which are inserted into the layered structure of MoS₂ to form 1T/2H phase polyphase MoS₂, consisting of 1T phase and 2H phase. The electrical conductivity of 1T/2H phase is greatly improved owing to the existence of the 1T phase. Furthermore, the combination with 2H phase helps to stabilize the metastable 1T phase and avoids the re-accumulation and transition to 2H phase. The transition from 1T/2H MoS₂ to 2H MoS₂ is by annealing treatment. The synthesis principle of CF@1T/2H MoS₂ is similar to that of 1T/2H MoS₂, as shown in Scheme 1b. Considering the advantages of 1T/2H MoS₂, the carbon fiber is chosen as a flexible substrate to obtain high-performance flexible EMW absorbing film.



Scheme 1 Schematic drawings illustrating the fabrication process of single MoS₂ (1T/2H MoS₂ and 2H MoS₂) and flexible CF/MoS₂ film (CF@1T/2H MoS₂ and CF@2H MoS₂)

The X-ray diffraction (XRD) patterns of MoS₂ samples with different phases are shown in Fig. 1a. Obviously, the 1T/2H MoS₂ and 2H MoS₂ have different XRD patterns. The (002) crystal-peaks value of 2H MoS₂ located at 14.4°, corresponds to the standard 2H phase bulk MoS₂ (PDF card #75-1539) [35, 36]. As for 1T/2H MoS₂, the corresponding (002) crystal peaks are situated at 2θ = 9.5° and 15.9°, and the *d* spacing difference between two (002) peaks proves the interlayer expansion. To further analyze the sample structure, Raman spectroscopy is introduced between 100 and 600 cm⁻¹, as shown in Fig. 1b. The intensity ratio of peak E_{1g} , E_{2g}^1 , and A_{1g} is situated at 284.7, 381.7, and 403.3, respectively. However, the intensity of E_{2g}^1 and A_{1g} peaks over 1T/2H MoS₂ is greatly decreased because of less 2H phase and worse crystallinity. As for 1T/2H MoS₂, the additional strong peaks at 150.3 (J1), 215.6 (J2), and 336.8 (J3) cm⁻¹ are observed, suggesting the formation of 1T phase MoS₂. After annealing, the J1, J2, and J3 peaks of the 1T phase become very weak, and E_{1g} , E_{2g}^1 , and A_{1g} peaks of the 2H phase become more significant, indicating that the 1T phase is successfully converted to the stable 2H phase. X-ray photoelectron spectrometer (XPS) displays the element content on the material surface. In Fig. 1c, the two peaks located at around 229 and 232 eV correspond to the spectra of Mo 3d_{5/2} and Mo 3d_{3/2}, clarifying the existence of 2H phase [37]. The peak at 226 eV corresponds to the spectra of S 2s. Moreover, as for 1T/2H MoS₂, two other peaks around 228 and 231 eV are observed, which have the 1 eV shift compared to that of 2H MoS₂, proving the presence of

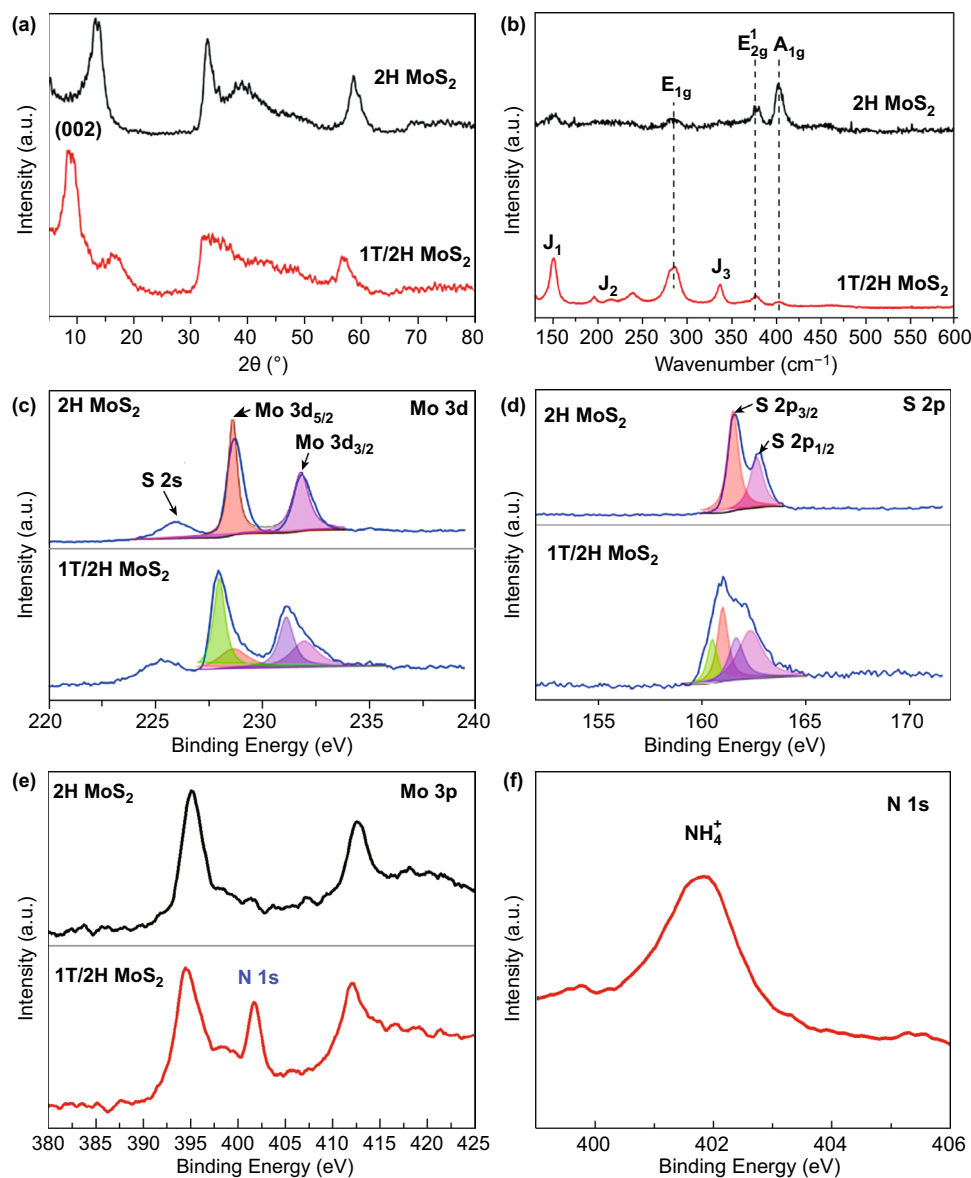


Fig. 1 **a** XRD patterns, **b** XPS spectra, **c** Mo 3d spectra, **d** S 2p spectra, **e** Mo 3p spectra of 1T/2H MoS₂ and 2H MoS₂. **f** N 1s spectra of 1T/2H MoS₂

the metallic 1T phase [38, 39]. Similarly, the two peaks can be observed at around 162.7 and 161.6 eV corresponding to the spectra of S 2p_{1/2} and S 2p_{3/2} (Fig. 1d). However, two additional peaks are found to shift to lower binding energies at around 161 and 160.5 eV, which once again suggests the presence of metallic 1T phase [39]. The content of 1T phase is estimated to be 61% by calculating the peak area. In Fig. 1e, the N 1s in the Mo 3p spectra of 1T/2H MoS₂ demonstrates the presence of the N element in 1T/2H MoS₂. But no N element can be detected after annealing in 2H MoS₂.

The peak at around 402 eV corresponding to the spectra of the N 1s in Fig. 1f should be attributed to the intercalation of NH₄⁺.

Figure 2 shows the SEM and TEM images of synthesized 1T/2H MoS₂. The SEM image (Fig. 2a) demonstrates that the 1T/2H MoS₂ is made up of an infinite number of tiny nanosheets, which is more clearly revealed by the TEM image in Fig. 2b, c. The crosswise dimension of each lamellar is approximately 80 nm. The high-resolution TEM image (Fig. 2d) confirms the co-existence of the trigonal prismatic

2H phase and the octahedral 1T phase in 1T/2H MoS₂. Furthermore, the lateral heterostructures of 1T (Fig. 2e) and 2H (Fig. 2f) phases could also be clearly visualized by zooming in the selected area of Fig. 2d. The element mapping images and EDX (Fig. S1) of 1T/2H MoS₂ demonstrate the uniform distribution of Mo and S elements. The N in the mapping of 1T/2H MoS₂ also demonstrates the presence of the N element in 1T/2H MoS₂, which is consistent with the XPS results. After annealing, the absence of N of the annealed 2H MoS₂ as revealed by Fig. S2, the morphology and microstructure of 2H MoS₂ are observed as shown in Fig. S3. On macroscopic view, the 2H MoS₂ remains the same morphology of 1T/2H MoS₂, but only the 2H phase can be found in the zoom HRTEM Fig. S3d, which demonstrates 1T phase

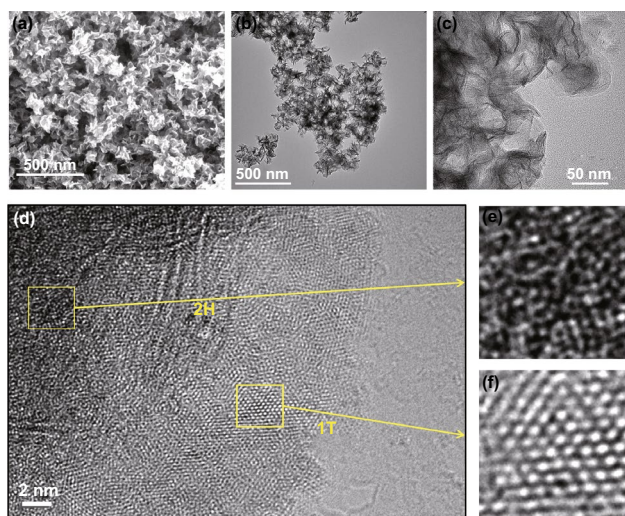


Fig. 2 a SEM image, b, c TEM image, d HRTEM images of 1T/2H MoS₂, e, f Enlarged images of the selected yellow area

is transformed into 2H phase under annealing condition completely.

To meet the demand of portable microwave absorption electronic devices, high-performance flexible film absorbers are urgently needed to be developed. Inspired by the synthetic methods of single 1T/2H MoS₂ and 2H MoS₂, the CF is added to the experiment as a substrate to obtain the flexible CF@1T/2H MoS₂ and CF@2H MoS₂ films. The XRD pattern and Raman spectrum of sample are shown in Fig. 3. In Fig. 3a, the CF@1T/2H MoS₂ and CF@2H MoS₂ have the same peaks as previous 1T/2H MoS₂ and CF@2H MoS₂ except the peak of carbon. As for Fig. 3b, the intensity ratio of peak D and G, situated at 1350 and 1580 cm⁻¹, respectively, the characteristic peak of carbon material, can reflect the presence of carbon fiber. In this figure, the peaks of MoS₂ are not obvious because the intensity of D peak and G peak is too high. After zooming the area of 150–600 cm⁻¹, the E_{1g}, E_{2g}¹, A_{1g} in both CF@1T/2H MoS₂ and CF@2H MoS₂, the J1, J2, J3 peaks in CF@1T/2H MoS₂ are the same as those in Fig. 1b.

To prove the microstructure and morphology of the obtained materials even further, SEM and TEM are also used to study the specific information of pure CF, CF@1T/2H MoS₂, and CF@2H MoS₂. The bare carbon fibers are made up of countless 400-nm-thin fibers, as shown in Fig. S4. The CF cloth has good flexibility and can be easily bent. After in situ growth of the CF@1T/2H MoS₂ and CF@2H MoS₂, it is easily seen that many sheets are coated on the surface of carbon fibers from Figs. 4 and S5, which turns out the same way that we did before to synthesize 1T/2H MoS₂ and CF@2H MoS₂ can also be used to synthesize flexible CF-based material. The presence of oxygen element in Fig. 4c comes from CF. Moreover,

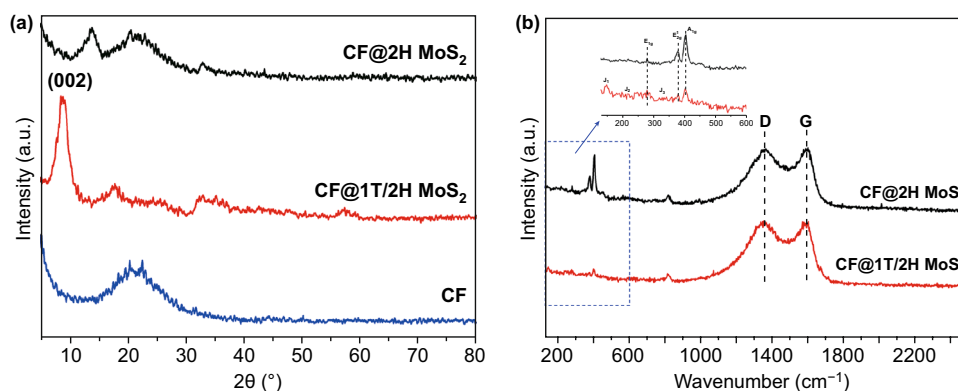


Fig. 3 a XRD patterns, b Raman spectroscopy of CF@1T/2H MoS₂ and CF@2H MoS₂



a large interlayer spacing of 9.3 Å is also observed in Fig. 4f, which should be attributed to the insertion of guest ions or molecules [24].

3.2 Electromagnetic Performance and Parameter

The coaxial transmission line method is adopted with aid of a vector network analyzer to obtain the EM parameters. First, the samples are mixed with paraffin with different mass ratio under 70 °C and then compressed into rings with natural cooling (diameter of the rings: $\varphi_{\text{ext}} = 7.00$ mm, $\varphi_{\text{int}} = 3.0$ mm.) Normally, as for an absorber, the absorption strength mainly depends on the magnetic loss and dielectric loss, which are defined by the complex permeability (μ_r) and permittivity (ϵ_r) [40–42]:

$$\epsilon_r = \epsilon' - j\epsilon'' \quad (1)$$

$$\mu_r = \mu' - j\mu'' \quad (2)$$

$$\tan\delta_\epsilon = \epsilon''/\epsilon' \quad (3)$$

$$\tan\delta_\mu = \mu''/\mu' \quad (4)$$

Generally speaking, the real and imaginary part indicate energy storage and energy loss, $\tan\delta_\epsilon$ represents the ratio of energy loss capability to storage capability [43, 44]. In order to effectively explore the influence of different phase on the electromagnetic properties of MoS₂, we measured the electromagnetic parameters of the 1T/2H MoS₂ and 2H MoS₂ with six kinds of proportion; the sample filling mass ratios in sample-paraffin mixture are 50%, 40%, 30%, 20%, 15%, and 10%. As shown in Fig. 5a, as for 1T/2H MoS₂, the ϵ' of six ratio 50%, 40%, 30%, 20%, 15%, and 10% are 12, 10.17, 9.16, 5.86, 4.31, and 3.59, respectively. As for 2H MoS₂, the ϵ' of six ratios 50%, 40%, 30%, 20%, 15%, and 10% are 4.2, 3.67, 3.13, 2.8, 2.7, and 2.6, respectively. More broadly, all the initial values of two samples both display the downward trend because MoS₂ is a single dielectric loss type material. Thus, ϵ' values naturally decrease as the sample proportion decreases. Moreover, the matrix loading percentage—initial ϵ'' curve of 1T/2H MoS₂ and 2H MoS₂, is shown in Fig. S6a. As matrix loading percentage goes down, so does initial ϵ'' values. The initial ϵ'' curve of 1T/2H MoS₂ is still higher than 2H MoS₂ at the same sample proportion. The all six ϵ' , ϵ'' and $\tan\delta_\epsilon$ curves of 1T/2H MoS₂ and 2H MoS₂ are shown in Fig. S7. Overall, all ϵ' , ϵ'' and $\tan\delta_\epsilon$ values of 1T/2H MoS₂ are higher than the 2H MoS₂ under the same sample ratio

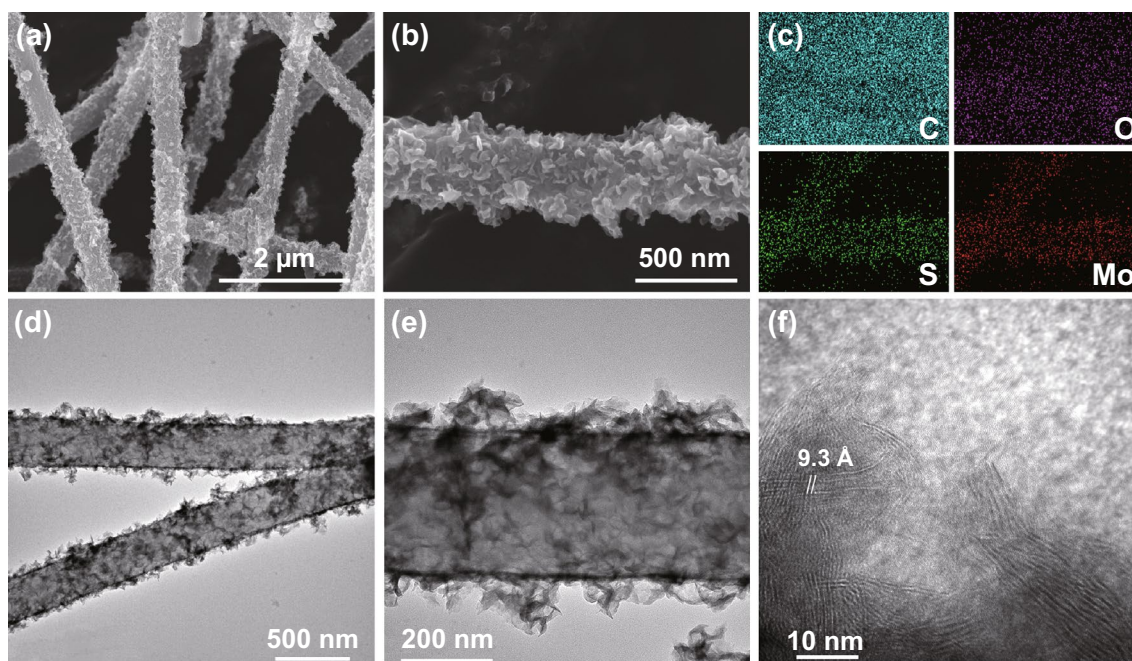


Fig. 4 a, b SEM image, c element mapping of C, O, S, Mo, d, e TEM image, f HRTEM images of CF@1T/2H MoS₂

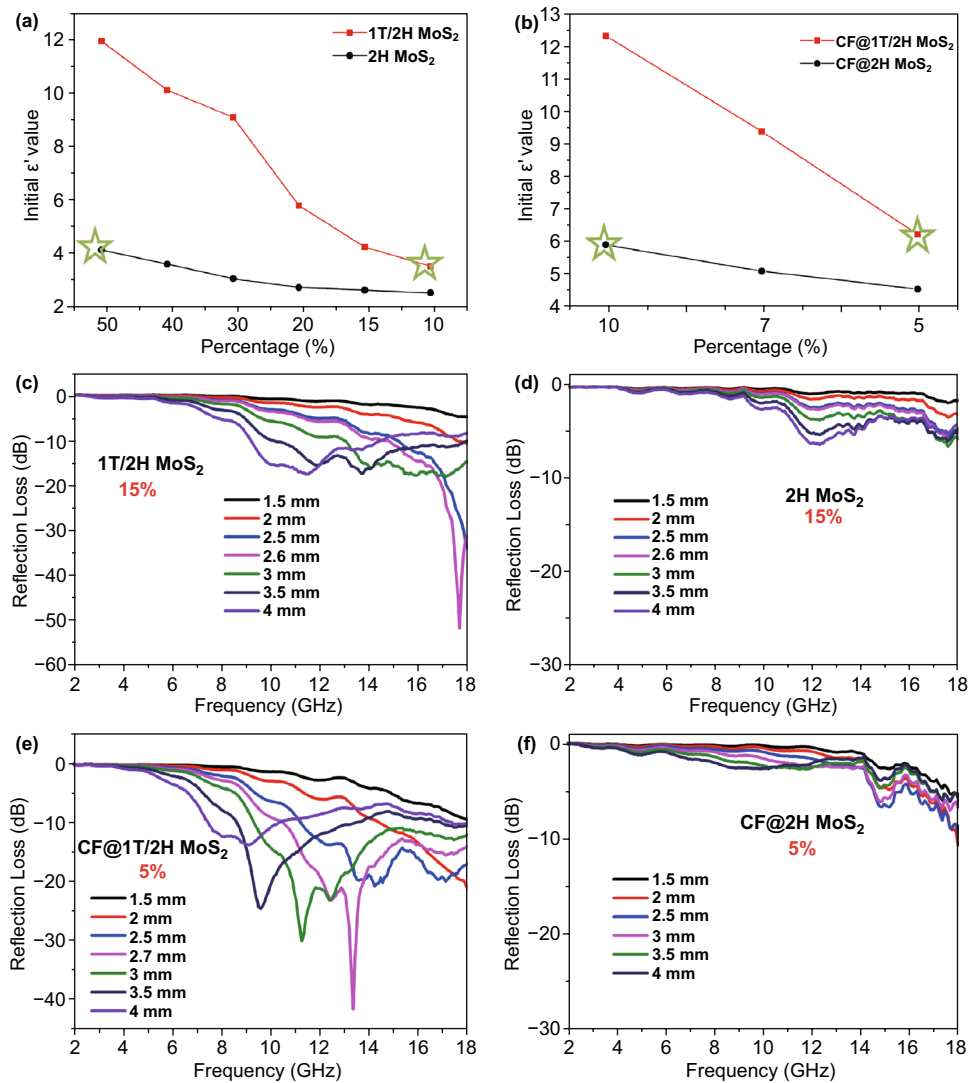


Fig. 5 a, b Matrix loading percentage–initial ϵ' of 1T/2H MoS₂ and 2H MoS₂, CF@1T/2H MoS₂ and CF@2H MoS₂. c, d Calculated reflection loss of 1T/2H MoS₂ and 2H MoS₂ with the matrix loading of 15wt%. e, f CF@1T/2H MoS₂ and CF@2H MoS₂ with the matrix loading of 5wt%

owing to the high electrical conductivity of 1T/2H MoS₂. The conductivity of 1T/2H MoS₂ and 2H MoS₂ measured by four-point probe is 9×10^{-2} and 1.515×10^{-2} , respectively, as shown in Fig. S9. The high conductivity of 1T/2H MoS₂ not only can produce the more conduction loss, but also can improve the dielectric property compared with 2H MoS₂. To be sure, the μ' and μ'' values of single dielectric loss type material are the constant value 1 and 0, respectively.

After adding CF, the study sample filling ratio is decreased because CF is also a high-dielectric loss type material. The final study ratios of CF@1T/2H MoS₂ and CF@2H MoS₂ are 10%, 7%, 5%. In Fig. 5b, the initial ϵ' of 10%, 7%, 5%

CF@1T/2H MoS₂ are 12.2, 9.26, 6.1, respectively. Comparatively, the initial ϵ' of 10%, 7%, 5% CF@2H MoS₂ are 5.78, 4.97, 4.42, respectively. From Fig. S5b, we can also draw the same conclusion of the initial ϵ'' of CF@1T/2H MoS₂ with 10%, 7%, and 5% ratios higher than the CF@2H MoS₂ with 10%, 7%, and 5% ratios. The all three ϵ' , ϵ'' , and $\tan \delta_e$ curves of CF@1T/2H MoS₂ and CF@2H MoS₂ are shown in Fig. S8a-f. From the result, we can find even the initial ϵ' value of 10% ratio CF@1T/2H MoS₂ higher than 50% ratio single 1T/2H MoS₂, which highlights the role of flexible CF. Furthermore, the conductivity of pure CF, CF@2H MoS₂, and CF@1T/2H MoS₂ measured by four-point probe

are 1.5×10^{-1} , 2.257×10^{-1} , and 5.298×10^{-1} , respectively, as shown in Fig. S9, consistent with the result of high initial ϵ' value of 10 wt% CF@1T/2H MoS₂.

The calculation of reflection loss can be based on the theory of electromagnetic wave transmission line, as shown in the following formula [45–47]:

$$R_L(\text{dB}) = 20 \log_{10} \left| \frac{Z_{\text{in}} - Z_0}{Z_{\text{in}} + Z_0} \right| \quad (5)$$

$$Z_{\text{in}} = Z_0 \sqrt{\mu_r/\epsilon_r} \tanh \left[j(2\pi f d/c) \sqrt{\mu_r \epsilon_r} \right] \quad (6)$$

Among them, Z_{in} refers to the normalized input impedance of electromagnetic wave absorbing materials; Z_0 refers to the impedance matching value in free space; f refers to the frequency of incident electromagnetic wave; d refers to the thickness of absorbing material; c refers to the propagation speed of electromagnetic wave. From Fig. 5c, d, as for the 15% filler loading of single MoS₂, the more intuitive information can be obtained. As for 1T/2H MoS₂, when the thickness is 2.6 mm, the minimum reflection loss ($R_{L\text{min}}$) value of 1T/2H MoS₂ can reach -52.7 dB at 17.7 GHz. The EMW absorption performance of the sample 2H MoS₂ is shown in Fig. 5d. The 2H MoS₂ with 15% filler loading is almost impossible to achieve electromagnetic absorption because the low ϵ' value. Herein, if $R_L = -10$ dB at a certain frequency, the material can absorb 90% wave, which can be considered effective absorption. The region R_L below -10 dB is called effective absorption bandwidth (EAB) [48, 49]. By contrast, the 2H MoS₂ with high filler loading (50%) can exhibit a good EMW absorbing performance, as shown in Fig. S10. The $R_{L\text{min}}$ is -60 dB when the thickness is 2.8 mm. Though 2H MoS₂ also can behave effective EMW absorption, it is limited by big filler loading. In general, the 1T/2H MoS₂ has a better electromagnetic absorption performance.

Figure 5e, f reflects the reflection loss of CF@1T/2H MoS₂ and CF@2H MoS₂ with the 5% filler loading. When the thickness is 2.7 mm, the $R_{L\text{min}}$ value of CF@1T/2H MoS₂ can reach -43 dB at 13.4 GHz only with 5% filler loading. Comparatively, the CF@2H MoS₂ with 5% filler loading is almost impossible to achieve electromagnetic absorption. This result reasserts the superiority of 1T/2H MoS₂.

In order to better reveal the EMW absorbing abilities of different phase, the 3D classical R_L - f diagram (Fig. 6) can make a more intuitive comparison between the two kinds of

materials. As shown in Fig. 6b, the corresponding EAB of 1T/2H MoS₂ (15%) can reach 10.52 GHz when the thickness is from 1.5 to 4 mm, which is equivalent to a potential to absorb all waves in the X (8–12 GHz) and Ku (12–18 GHz) bands. As Fig. 6d shows, with the addition of CF, the EAB ranges from 9.25 to 18 GHz.

3.3 EMW Absorption Mechanism

The next step is to explore the electromagnetic absorption mechanism of 1T/2H phase MoS₂. As we know, good electromagnetic absorbing performance is closely related to the electromagnetic attenuation, more loss (here is dielectric loss) and good impedance matching. Firstly, the propagation paths of incident EMW inside MoS₂-based absorbers can be enhanced by scattering effect because of the extreme thinness and high specific surface area of MoS₂. Attenuation matching means the ability and speed to convert the energy of EM waves to other forms of energy. The higher the attenuation constant α is, the closer the material is to attenuation matching [50–52], and the specific formula is as follows:

$$\alpha = \frac{\sqrt{2}\pi f}{c} \times \sqrt{(\mu''\epsilon'' - \mu'\epsilon') + \sqrt{(\mu''\epsilon'' - \mu'\epsilon')^2 + (\mu'\epsilon'' + \mu''\epsilon')^2}} \quad (7)$$

In Fig. 7a, four curves rise by frequency, and with the addition of CF, all the curves are in order of height: CF@1T/2H MoS₂ (5%) \geq 1T/2H MoS₂ (15%) \geq CF@2H MoS₂ (5%) \geq 2H MoS₂ (15%). The maximum α value rises from 50 to 350. At their $R_{L\text{min}}$ point, α of CF@1T/2H MoS₂ (5%) is 236, larger than that of the CF@2H MoS₂ (5%). The α of 1T/2H MoS₂ (15%) is 73, still larger than that of the 2H MoS₂ (15%). This proves that the 1T/2H MoS₂ based material has good attenuation loss capacity.

The dielectric loss in 2–18 GHz is chiefly dominated by polarization relaxation. Figure 7b shows the Cole–Cole semicircle analyzing how many relaxation processes each material own. According to the Debye theory,

$$\left(\epsilon' - \frac{\epsilon_s + \epsilon_\infty}{2} \right)^2 + (\epsilon'')^2 = \left(\frac{\epsilon_s - \epsilon_\infty}{2} \right)^2 \quad (8)$$

When ϵ'' varies with ϵ' , every semicircle represents a relaxation process [53–55]. The arc could be regarded as a similar process. For the 1T/2H MoS₂, four processes are distinguished, while the CF@1T/2H MoS₂ has five. More

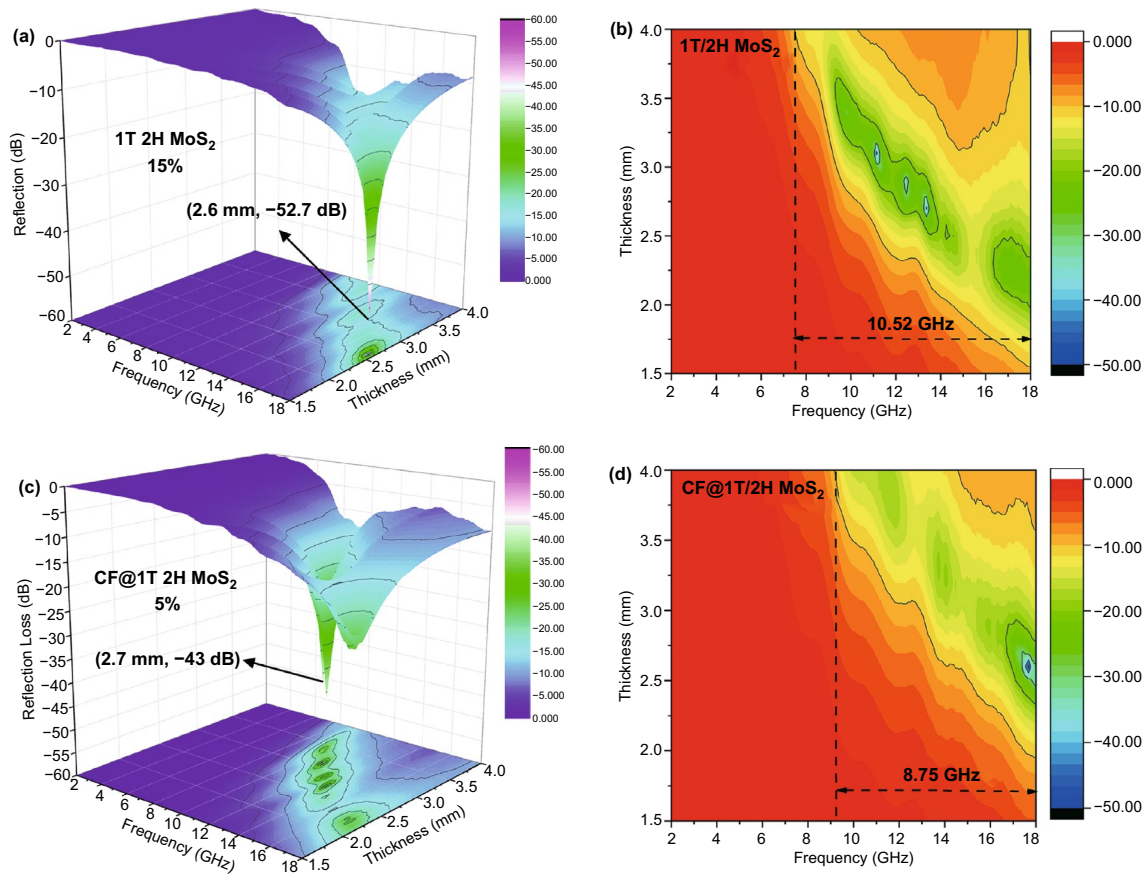


Fig. 6 a, c 3D reflection loss, b, d corresponding contour maps of 1T/2H MoS₂ (15%) and CF@1T/2H MoS₂ (5%)

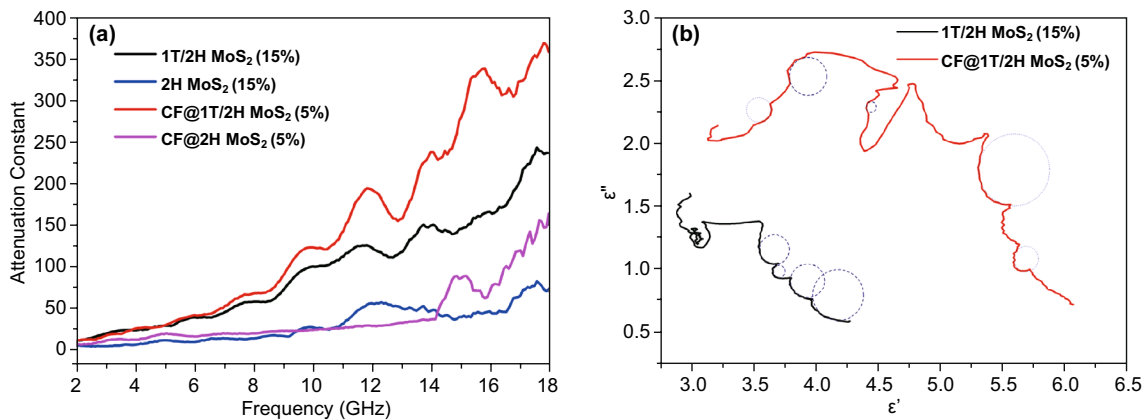


Fig. 7 a Attenuation constant of 1T/2H MoS₂ and 2H MoS₂ (15%), CF@1T/2H MoS₂ and CF@2H MoS₂ (5%). b Cole–Cole semicircle of 1T/2H MoS₂ (15%) and CF@1T/2H MoS₂ (5%)

processes supply more dielectric loss; thus, the CF@1T/2H MoS₂ has better dissipation ability.

To achieve an excellent absorption performance, the prerequisite is the less reflection, and zero reflection of

the incident microwave is the best. Based on the transmission line theory, if the minimum R_L could correspond to impedance matching ratio value ($Z=|Z_{in}/Z_0|$) equal 1 at the

same frequency, the impedance of this material matches well. The calculation formula is as follows [56–59]:

$$Z_{in} = Z_0 \sqrt{\mu_r / \epsilon_r} \tanh [j(2\pi f d / c) \sqrt{\mu_r \epsilon_r}] \quad (9)$$

The image in Fig. 8 displays the normalized input impedance of as-prepared samples. As we can see, the CF@1T/2H MoS₂ (2.7 mm) and 1T/2H MoS₂ (2.6 mm) meet this requirement, demonstrating the good impedance matching of 1T/2H MoS₂-based absorber.

When the thickness of the material is increasing, the frequency corresponding to minimum R_L becomes smaller. This regularity is in line with the $\lambda/4$ wave length model as follows [60–62]:

$$t_m = \frac{nc}{4f_m \sqrt{|\mu_r| |\epsilon_r|}} \quad (10)$$

When the value of t_m^{exp} just falls on the curve t_m^{fit} , the electromagnetic wave is canceled because the two reflected waves formed by air-absorber and the metal-absorption interface form 180° out of phase. In the middle image of Fig. 8,

all two curves of fit thickness decline with the increase in frequency. The circle marks correspond to the frequency that R_L is reaching the minimum. The 1T/2H MoS₂ (15%) and CF@1T/2H MoS₂ (5%) perfectly fit the model by realizing the equality of two thicknesses of 2.6 and 2.7 mm, respectively. In total, considering the high dielectric loss result from better conductivity, big attenuation, good impedance matching and low filler loading, the as-prepared 1T/2H MoS₂ is expected to exhibit excellent EMW absorbing abilities. Compared with the previous MoS₂-based EMW absorbers, as shown in Table 1, the 1T/2H MoS₂ and CF@1T/2H MoS₂ can achieve the effective electromagnetic absorption only with low filler loading (15%) and (5%), respectively.

3.4 Radar Cross Section

When the geometrical shape of the absorbing material is stable, the radar cross section (RCS) is an important index to judge the absorbing ability of the absorbing material [63, 64]. The HFSS simulation is used to explore the RCS

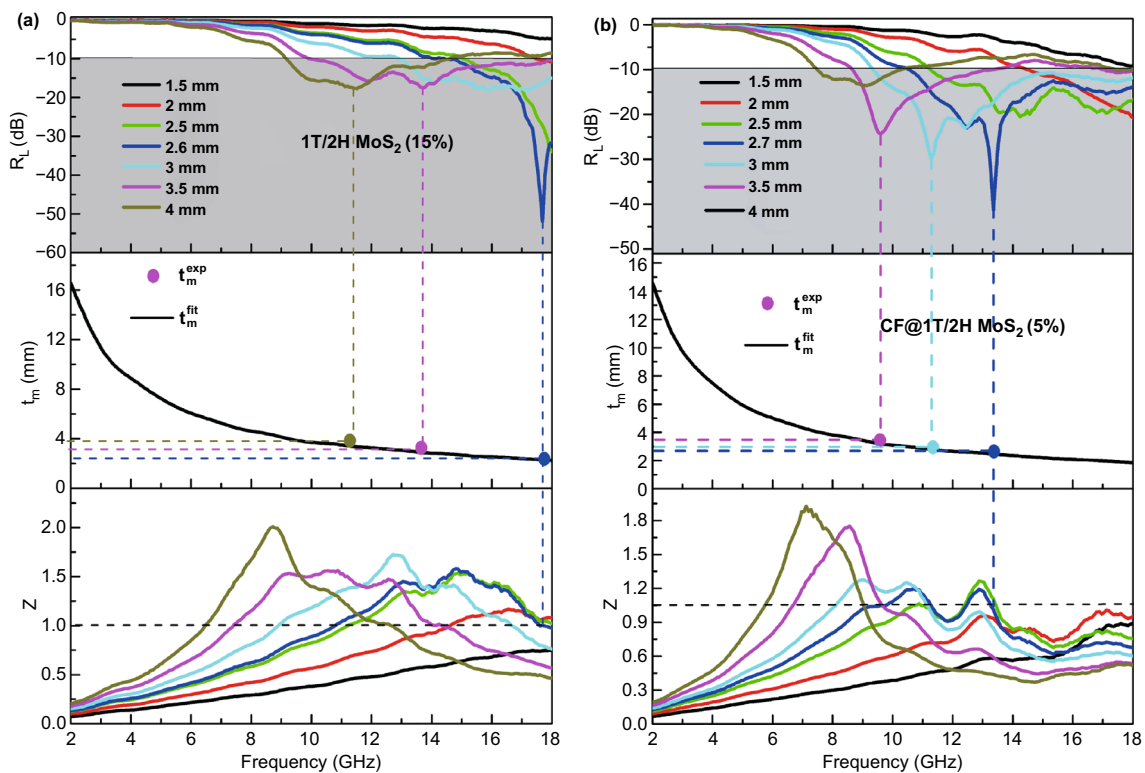


Fig. 8 Dependence of the matching thickness (t_m) on frequency (f_m) under $\lambda/4$ and normalized input impedance of 1T/2H MoS₂ (15%) and CF@1T/2H MoS₂ (5%)

Table 1 Summary of MoS₂-based EMW absorbers

Material	Ratio	Thickness (mm)	EAB (GHz) ($R_L \leq -10$ dB)	R_{Lmin} (dB)	Refs.
PB@ MoS ₂	40%	2.4	10.2	-42.83	[14]
CNTs@MoS ₂	40%	1.5	4	-35	[15]
CoFe ₂ O ₄ @1T/2H-MoS ₂	40%	1.81	14.5	-68.5	[27]
MoS ₂	60%	2.4	7.44	-47.8	[28]
MoS ₂ -NS	60%	2.4	9.36	-38.42	[29]
1T/2H MoS ₂ @RGO	30%	2.5	4	-67.77	[31]
1T/2H MoS ₂ work	15%	2.6	10.52	-52.7	This work
CF@1T/2H MoS ₂	5%	2.7	8.75	-43	This work

performance of CF@1T/2H MoS₂ and 1T/2H MoS₂. The aluminum (Al) plate is used as the substrate and set to a thin

tube with 180 mm long and 5 mm thick [65]. The prepared samples are mixed with paraffin as the absorber coating;

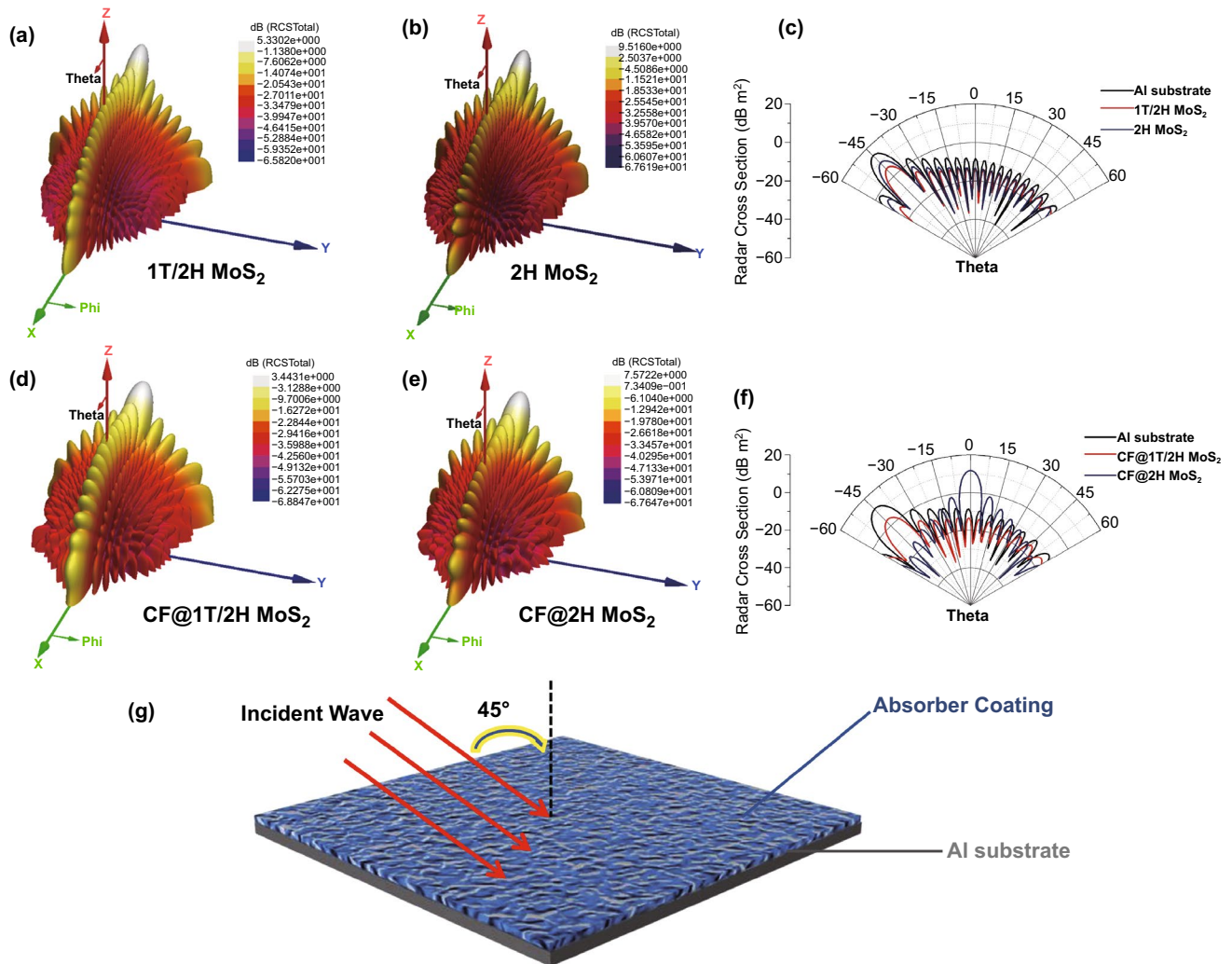


Fig. 9 a, b, d, e Three-dimensional spherical coordinate diagrams. c, f Polar coordinate diagram. g Schematic diagram of HFSS simulation analysis

it has the same length as the Al plate but the thickness is chosen the above calculated thickness value corresponding to the optimum EMW absorbing performance. In this work, the thickness of 1T/2H MoS₂ is 2.6 mm, the thickness of CF@1T/2H MoS₂ is 2.7 mm, and the schematic diagram is shown in Fig. 9g. The incident direction of EM wave is oblique at 45°, the calculation can begin when the material is given an appropriate excitation boundary. After simulation calculations, the RCS values of Al plate and different absorbers are obtained. The 3D spherical coordinate diagrams in different directions and polar plots between -60°–60° are shown in Fig. 9a–f. It can be seen that when the EMW is incident on the Al plate coated with MoS₂ absorber/paraffin mixture, the RCS values are smaller than that of single Al plate. In particular, the RCS values of 1T/2H MoS₂ are smaller than 2H MoS₂, which further proves the superiority of 1T/2H MoS₂ as electromagnetic wave absorber. As for CF@1T/2H MoS₂ and CF@2H MoS₂, we can also draw a conclusion that the RCS values of CF@1T/2H MoS₂ are smaller than CF@2H MoS₂. In summary, the absorbers of 1T/2H MoS₂ based material exhibit excellent EMW absorption performance.

4 Conclusion

In this work, we successfully synthesize the 1T/2H MoS₂ and 2H MoS₂ through a facile hydrothermal route and profoundly explore the influence of different MoS₂ phase for electromagnetic absorbing properties by analyzing electromagnetic parameters of 1T/2H MoS₂ and 2H MoS₂ with 50%, 40%, 30%, 20%, 15%, and 10% filler loading. As a result, the R_{Lmin} of 1T/2H MoS₂ only with 15% filler loading can reach -52.7 dB at 17.7 GHz when the thickness is 2.6 mm. The excellent EMW absorption performance of 1T/2H MoS₂ than 2H MoS₂ is due to the high dielectric loss result from better conductivity, big attenuation and good impedance matching. In addition, taking the advantage of 1T/2H MoS₂, the flexible CF@1T/2H MoS₂ is also synthesized to mind the request of flexible portable microwave absorption electronic devices. When the thickness is 2.7 mm, the R_{Lmin} value of CF@1T/2H MoS₂ can reach -43 dB at 13.4 GHz only with 5% filler loading.

Acknowledgments The work was supported by the National Natural Science Foundation of China (No. 51672222), Joint Fund

Project-Enterprise-Shaanxi Coal Joint Fund Project (2019JLM-32), Innovation Foundation for Doctor Dissertation of Northwestern Polytechnical University (CX202054) and the Graduate innovation team of Northwestern Polytechnical University. The authors thank the Analysis and Testing Center of Northwestern Polytechnical University for their technical assistance in SEM (Verios G4).

Open Access This article is licensed under a Creative Commons Attribution 4.0 International License, which permits use, sharing, adaptation, distribution and reproduction in any medium or format, as long as you give appropriate credit to the original author(s) and the source, provide a link to the Creative Commons licence, and indicate if changes were made. The images or other third party material in this article are included in the article's Creative Commons licence, unless indicated otherwise in a credit line to the material. If material is not included in the article's Creative Commons licence and your intended use is not permitted by statutory regulation or exceeds the permitted use, you will need to obtain permission directly from the copyright holder. To view a copy of this licence, visit <http://creativecommons.org/licenses/by/4.0/>.

Supplementary Information The online version contains supplementary material available at <https://doi.org/10.1007/s40820-021-00646-y>.

References

1. R.C. Che, L.M. Peng, X.F. Duan, Q. Chen, X. Liang, Microwave absorption enhancement and complex permittivity and permeability of Fe encapsulated within carbon nanotubes. *Adv. Mater.* **16**(5), 401–405 (2004). <https://doi.org/10.1002/adma.200306460>
2. H. Lv, Z. Yang, P.L. Wang, G. Ji, J. Song et al., A voltage-boosting strategy enabling a low-frequency, flexible electromagnetic wave absorption device. *Adv. Mater.* **30**(15), 1706343 (2018). <https://doi.org/10.1002/adma.201706343>
3. Q. Liu, Q. Cao, H. Bi, C. Liang, K. Yuan et al., CoNi@SiO₂@TiO₂ and CoNi@Air@TiO₂ microspheres with strong wideband microwave absorption. *Adv. Mater.* **28**(3), 486–490 (2016). <https://doi.org/10.1002/adma.201503149>
4. M.S. Cao, X.X. Wang, W.Q. Cao, X.Y. Fang, B. Wen et al., Thermally driven transport and relaxation switching self-powered electromagnetic energy conversion. *Small* **14**(29), 1800987 (2018). <https://doi.org/10.1002/sml.201800987>
5. P. Liu, C. Zhu, S. Gao, C. Guan, Y. Huang et al., N-doped porous carbon nanoplates embedded with CoS₂ vertically anchored on carbon cloths for flexible and ultrahigh microwave absorption. *Carbon* **163**, 348–359 (2020). <https://doi.org/10.1016/j.carbon.2020.03.041>
6. M.S. Cao, X.X. Wang, M. Zhang, W.Q. Cao, X.Y. Fang et al., Variable-temperature electron transport and dipole polarization turning flexible multifunctional microsensor beyond electrical and optical energy. *Adv. Mater.* **32**(10), 1907156 (2020). <https://doi.org/10.1002/adma.201907156>

7. J. Yan, Y. Huang, C. Wei, N. Zhang, P. Liu, Covalently bonded polyaniline/graphene composites as high-performance electromagnetic (EM) wave absorption materials. *Compos. Pt. A-Appl. Sci. Manuf.* **99**, 121–128 (2017). <https://doi.org/10.1016/j.compositesa.2017.04.016>
8. R. Shu, G. Zhang, C. Zhang, Y. Wu, J. Zhang, Nitrogen-doping-regulated electromagnetic wave absorption properties of ultralight three-dimensional porous reduced graphene oxide aerogels. *Adv. Electron. Mater.* **7**, 2001001 (2020). <https://doi.org/10.1002/aelm.202001001>
9. D. Zhang, T. Liu, J. Cheng, Q. Cao, G. Zheng et al., Light-weight and high-performance microwave absorber based on 2D WS₂-RGO heterostructures. *Nano-Micro Lett.* **11**(1), 38 (2019). <https://doi.org/10.1007/s40820-019-0270-4>
10. B. Wen, M. Cao, M. Lu, W. Cao, H. Shi et al., Reduced graphene oxides: light-weight and high-efficiency electromagnetic interference shielding at elevated temperatures. *Adv. Mater.* **26**(21), 3484–3489 (2014). <https://doi.org/10.1002/adma.201400108>
11. T. Zhu, W. Shen, X. Wang, Y.F. Song, W. Wang, Paramagnetic CoS₂@MoS₂ core-shell composites coated by reduced graphene oxide as broadband and tunable high-performance microwave absorbers. *Chem. Eng. J.* **378**, 122159 (2019). <https://doi.org/10.1016/j.cej.2019.122159>
12. L. Gai, Y. Zhao, G. Song, Q. An, Z. Xiao et al., Construction of core-shell PPy@ MoS₂ with nanotube-like heterostructures for electromagnetic wave absorption: assembly and enhanced mechanism. *Compos. Pt. A-Appl. Sci. Manuf.* **136**, 105965 (2020). <https://doi.org/10.1016/j.compositesa.2020.105965>
13. M. Ning, Q. Man, G. Tan, Z. Lei, J. Li et al., Ultrathin MoS₂ nanosheets encapsulated in hollow carbon spheres: a case of a dielectric absorber with optimized impedance for efficient microwave absorption. *ACS Appl. Mater. Interfaces* **12**(18), 20785–20796 (2020). <https://doi.org/10.1021/acsami.9b20433>
14. Z. Zhao, S. Xu, Z. Du, C. Jiang, X. Huang et al., Metal-organic framework-based PB@MoS₂ core-shell microcubes with high efficiency and broad bandwidth for microwave absorption performance. *ACS Sustain. Chem. Eng.* **7**(7), 7183–7192 (2019). <https://doi.org/10.1021/acssuschemeng.9b00191>
15. R. Wang, E. Yang, X. Qi, R. Xie, S. Qin et al., Constructing and optimizing core@ shell structure CNTs@MoS₂ nanocomposites as outstanding microwave absorbers. *Appl. Surface Sci.* **516**, 146159 (2020). <https://doi.org/10.1016/j.apsusc.2020.146159>
16. M.S. Cao, Y.Z. Cai, P. He, J.C. Shu, W.Q. Cao et al., 2D MXenes: electromagnetic property for microwave absorption and electromagnetic interference shielding. *Chem. Eng. J.* **359**, 1265–1302 (2019). <https://doi.org/10.1016/j.cej.2018.11.051>
17. Y. Li, F. Meng, Y. Mei, H. Wang, Y. Guo et al., Electrospun generation of Ti₃C₂T_x MXene@graphene oxide hybrid aerogel microspheres for tunable high-performance microwave absorption. *Chem. Eng. J.* **391**, 123512 (2020). <https://doi.org/10.1016/j.cej.2019.123512>
18. J. Wang, L. Liu, S. Jiao, K. Ma, J. Lv, Hierarchical carbon fiber@MXene@MoS₂ core-sheath synergistic microstructure for tunable and efficient microwave absorption. *Adv. Funct. Mater.* **30**(45), 2002595 (2020). <https://doi.org/10.1002/adfm.202002595>
19. X. Gao, B. Wang, K. Wang, S. Xu, S. Liu et al., Design of Ti₃C₂T_x/TiO₂/PANI multi-layer composites for excellent electromagnetic wave absorption performance. *J. Colloid Interface Sci.* **583**, 510–521 (2021). <https://doi.org/10.1016/j.jcis.2020.09.094>
20. W. Wu, L. Wang, R. Yu, Y. Liu, S.H. Wei et al., Piezophotonic effect in single-atomic-layer MoS₂ for strain-gated flexible optoelectronics. *Adv. Mater.* **28**(38), 8463–8468 (2016). <https://doi.org/10.1002/adma.201602854>
21. Q.H. Wang, K. Kalantar Zadeh, A. Kis, J.N. Coleman, M.S. Strano, Electronics and optoelectronics of two-dimensional transition metal dichalcogenides. *Nat. Nanotechnol.* **7**(11), 699–712 (2012). <https://doi.org/10.1038/nnano.2012.193>
22. Z.A. Ghazi, X. He, A.M. Khattak, N.A. Khan, B. Liang et al., MoS₂/celgard separator as efficient polysulfide barrier for long-life lithium-sulfur batteries. *Adv. Mater.* **29**(21), 1606817 (2017). <https://doi.org/10.1002/adma.201606817>
23. J. Ru, T. He, B. Chen, Y. Feng, L. Zu et al., Covalent assembly of MoS₂ nanosheets with SnS nanodots as linkages for lithium/sodium-ion batteries. *Angew. Chem. Int. Ed.* **59**(34), 14621–14627 (2017). <https://doi.org/10.1002/anie.202005840>
24. D. Wang, X. Zhang, S. Bao, Z. Zhang, H. Fei et al., Phase engineering of a multiphase 1T/2H MoS₂ catalyst for highly efficient hydrogen evolution. *J. Mater. Chem. A* **5**(6), 2681–2688 (2017). <https://doi.org/10.1039/C6TA09409K>
25. Q. Jin, N. Liu, C. Dai, R. Xu, B. Wu et al., H₂-directing strategy on in situ synthesis of Co-MoS₂ with highly expanded interlayer for elegant HER activity and its mechanism. *Adv. Energy Mater.* **10**(20), 2000291 (2020). <https://doi.org/10.1002/aenm.202000291>
26. M. Chhowalla, H.S. Shin, G. Eda, L.J. Li, K.P. Loh et al., The chemistry of two-dimensional layered transition metal dichalcogenide nanosheets. *Nat. Chem.* **5**(4), 263–275 (2013). <https://doi.org/10.1038/nchem.1589>
27. X. Wang, T. Zhu, S. Chang, Y. Lu, W. Mi et al., 3D nest-like architecture of core-shell CoFe₂O₄@1T/2H-MoS₂ composites with tunable microwave absorption performance. *ACS Appl. Mater. Interfaces* **12**(9), 11252–11264 (2020). <https://doi.org/10.1021/acsami.9b23489>
28. X. Liang, X. Zhang, W. Liu, D. Tang, B. Zhang et al., A simple hydrothermal process to grow MoS₂ nanosheets with excellent dielectric loss and microwave absorption performance. *J. Mater. Chem. C* **4**(28), 6816–6821 (2016). <https://doi.org/10.1039/C6TC02006B>
29. M.Q. Ning, M.M. Lu, J.B. Li, Z. Chen, Y.K. Dou et al., Two-dimensional nanosheets of MoS₂: a promising material with high dielectric properties and microwave absorption performance. *Nanoscale* **7**(38), 15734–15740 (2015). <https://doi.org/10.1039/C5NR04670J>
30. L. Lyu, F. Wang, B. Li, X. Zhang, J. Qiao et al., Constructing 1T/2H MoS₂ nanosheets/3D carbon foam for high-performance electromagnetic wave absorption. *J. Colloid Interface*



- Sci. **586**, 613–620 (2020). <https://doi.org/10.1016/j.jcis.2020.10.129>
31. H. Guo, L. Wang, W. You, L. Yang, X. Li et al., Engineering phase transformation of MoS₂/RGO by N-doping as an excellent microwave absorber. *ACS Appl. Mater. Interfaces* **12**(14), 16831–16840 (2020). <https://doi.org/10.1021/acsami.0c01998>
 32. L. Ye, S. Chen, W. Li, M. Pi, T. Wu et al., Tuning the electrical transport properties of multilayered molybdenum disulfide nanosheets by intercalating phosphorus. *J. Phys. Chem. C* **119**(17), 9560–9567 (2015). <https://doi.org/10.1021/jp5128018>
 33. C.K. Chua, A.H. Loo, M. Pumera, Top-down and bottom-up approaches in engineering 1T phase molybdenum disulfide (MoS₂): towards highly catalytically active materials. *Chem. A-Eur. J.* **22**(40), 14336–14341 (2016). <https://doi.org/10.1002/chem.201602764>
 34. M. Zhang, C. Han, W.Q. Cao, M.S. Cao, H.J. Yang et al., A nano-micro engineering nanofiber for electromagnetic absorber, green shielding and sensor. *Nano-Micro Lett.* **13**(1), 27 (2021). <https://doi.org/10.1007/s40820-020-00552-9>
 35. D. Zhang, J. Chai, J. Cheng, Y. Jia, X. Yang et al., Highly efficient microwave absorption properties and broadened absorption bandwidth of MoS₂-iron oxide hybrids and MoS₂-based reduced graphene oxide hybrids with Hetero-structures. *Appl. Surface Sci.* **462**, 872–882 (2018). <https://doi.org/10.1016/j.apsusc.2018.08.152>
 36. J. Chai, J. Cheng, D. Zhang, Y. Xiong, X. Yang et al., Enhancing electromagnetic wave absorption performance of Co₃O₄ nanoparticles functionalized MoS₂ nanosheets. *J. Alloy. Compd.* **829**, 154531 (2020). <https://doi.org/10.1016/j.jallcom.2020.154531>
 37. D. Wang, B. Su, Y. Jiang, L. Li, B.K. Ng et al., Polytype 1T/2H MoS₂ heterostructures for efficient photoelectrocatalytic hydrogen evolution. *Chem. Eng. J.* **330**, 102–108 (2017). <https://doi.org/10.1016/j.cej.2017.07.126>
 38. M. Acerce, D. Voiry, M. Chhowalla, Metallic 1T phase MoS₂ nanosheets as supercapacitor electrode materials. *Nat. Nanotechnol.* **10**(4), 313–318 (2015). <https://doi.org/10.1038/nnano.2015.40>
 39. G. Eda, H. Yamaguchi, D. Voiry, T. Fujita, M. Chen et al., Photoluminescence from chemically exfoliated MoS₂. *Nano Lett.* **11**(12), 5111–5116 (2011). <https://doi.org/10.1021/nl201874w>
 40. P. Liu, S. Gao, Y. Wang, F. Zhou, Y. Huang et al., Metal-organic polymer coordination materials derived Co/N-doped porous carbon composites for frequency-selective microwave absorption. *Compos. PT. B-Eng.* **202**, 108406 (2020). <https://doi.org/10.1016/j.compositesb.2020.108406>
 41. P. Liu, S. Gao, Y. Wang, Y. Huang, F. Zhou et al., Magnetic porous N-doped carbon composites with adjusted composition and porous microstructure for lightweight microwave absorbers. *Carbon* **173**, 655–666 (2021). <https://doi.org/10.1016/j.carbon.2020.11.043>
 42. J. Cheng, H. Zhang, Y. Xiong, L. Gao, B. Wen et al., Construction of multiple interfaces and dielectric/magnetic heterostructures in electromagnetic wave absorbers with enhanced absorption performance: a review. *J. Materiomics* (2021). <https://doi.org/10.1016/j.jmat.2021.02.017>
 43. Y. Cheng, J.Z.Y. Seow, H. Zhao, Z.J. Xu, G. Ji, A flexible and lightweight biomass-reinforced microwave absorber. *Nano-Micro Lett.* **12**(1), 125 (2020). <https://doi.org/10.1007/s40820-020-00461-x>
 44. P. Liu, S. Gao, Y. Wang, F. Zhou, Y. Huang et al., Core-shell Ni@C encapsulated by N-doped carbon derived from nickel-organic polymer coordination composites with enhanced microwave absorption. *Carbon* **170**, 503–516 (2020). <https://doi.org/10.1016/j.carbon.2020.08.043>
 45. L. Wang, B. Wen, H. Yang, Y. Qiu, N. He, Hierarchical nest-like structure of Co/Fe MOF derived CoFe@C composite as wide-bandwidth microwave absorber. *Compos. Pt. A-Appl. Sci. Manuf.* **135**, 105958 (2020). <https://doi.org/10.1016/j.compositesa.2020.105958>
 46. L. Wang, X. Bai, T. Zhao, Y. Lin, Facile synthesis of N, S-codoped honeycomb-like C/Ni₃S₂ composites for broadband microwave absorption with low filler mass loading. *J. Colloid Interface Sci.* **580**, 126–134 (2020). <https://doi.org/10.1016/j.jcis.2020.07.025>
 47. M. Ma, W. Li, Z. Tong, Y. Ma, Y. Bi et al., NiCo₂O₄ nanosheets decorated on one-dimensional ZnFe₂O₄@SiO₂@C nanochains with high-performance microwave absorption. *J. Colloid Interface Sci.* **578**, 58–68 (2020). <https://doi.org/10.1016/j.jcis.2020.05.044>
 48. X. Liang, Z. Man, B. Quan, J. Zheng, W. Gu et al., Environment-stable CoxNiy encapsulation in stacked porous carbon nanosheets for enhanced microwave absorption. *Nano-Micro Lett.* **12**(1), 102 (2020). <https://doi.org/10.1007/s40820-020-00432-2>
 49. M. Ma, W. Li, Z. Tong, Y. Yang, Y. Ma et al., 1D flower-like Fe₃O₄@SiO₂@MnO₂ nanochains inducing RGO self-assembly into aerogels for high-efficient microwave absorption. *Mater. Design* **188**, 108462 (2020). <https://doi.org/10.1016/j.matdes.2019.108462>
 50. J. Yan, Y. Huang, X. Liu, X. Zhao, T. Li et al., Polypyrrole-based composite materials for electromagnetic wave absorption. *Polym. Rev.* 1–42 (2020). <https://doi.org/10.1080/15583724.2020.1870490>
 51. J. Yan, Y. Huang, Y. Yan, X. Zhao, P. Liu, The composition design of MOF-derived Co-Fe bimetallic autocatalysis carbon nanotubes with controllable electromagnetic properties. *Compos. Pt. A-Appl. Sci. Manuf.* **139**, 106107 (2020). <https://doi.org/10.1016/j.compositesa.2020.106107>
 52. X.Y. Wang, Y.K. Lu, T. Zhu, S.C. Chang, W. Wang, CoFe₂O₄/N-doped reduced graphene oxide aerogels for high-performance microwave absorption. *Chem. Eng. J.* **388**, 16 (2020). <https://doi.org/10.1016/j.cej.2020.124317>
 53. J. Qiao, X. Zhang, C. Liu, L.F. Luy, Y.F. Yang, Z. Wang et al., (2021) Non-magnetic bimetallic MOF-derived porous carbon-wrapped TiO₂/ZrTiO₄ composites for efficient electromagnetic wave absorption. *Nano-Micro Lett.* **13**, 75 (2021). <https://doi.org/10.1007/s40820-021-00606-6>
 54. S. Gao, S.H. Yang, H.Y. Wang, G.S. Wang, P.G. Yin, Excellent electromagnetic wave absorbing properties of

- two-dimensional carbon-based nanocomposite supported by transition metal carbides Fe_3C . *Carbon* **162**, 438–444 (2020). <https://doi.org/10.1016/j.carbon.2020.02.031>
55. T. Zhu, S.C. Chang, Y.F. Song, M. Lahoubi, W. Wang, PVP-encapsulated $\text{CoFe}_2\text{O}_4/\text{rGO}$ composites with controllable electromagnetic wave absorption performance. *Chem. Eng. J.* **373**, 755–766 (2019). <https://doi.org/10.1016/j.cej.2019.05.079>
56. Y.L. Wang, S.H. Yang, H.Y. Wang, G.S. Wang, X.B. Sun et al., Hollow porous CoNi/C composite nanomaterials derived from MOFs for efficient and lightweight electromagnetic wave absorber. *Carbon* **167**, 485–494 (2020). <https://doi.org/10.1016/j.carbon.2020.06.014>
57. G.H. He, Y.P. Duan, H.F. Pang, Microwave absorption of crystalline $\text{Fe}/\text{MnO}@\text{C}$ nanocapsules embedded in amorphous carbon. *Nano-Micro Lett.* **12**, 57 (2020). <https://doi.org/10.1007/s40820-020-0388-4>
58. X. Wang, J. Liao, R. Du, G. Wang, N. Tsidaeva et al., Achieving super-broad effective absorption bandwidth with low filler loading for graphene aerogels/raspberry-like CoFe_2O_4 clusters by N doping. *J. Colloid Interface Sci.* **590**, 186–198 (2021). <https://doi.org/10.1016/j.jcis.2021.01.069>
59. D. Zhang, Y. Xiong, J. Cheng, J. Chai, T. Liu et al., Synergetic dielectric loss and magnetic loss towards superior microwave absorption through hybridization of few-layer WS_2 nanosheets with NiO nanoparticles. *Sci. Bull.* **65**(2), 138–146 (2020). <https://doi.org/10.1016/j.scib.2019.10.011>
60. Y. Wang, X. Di, Z. Lu, X. Wu, Rational construction of hierarchical $\text{Co}@C@NPC$ nanocomposites derived from bimetallic hybrid ZIFs/biomass for boosting the microwave absorption. *J. Colloid Interface Sci.* **589**, 462–471 (2021). <https://doi.org/10.1016/j.jcis.2021.01.013>
61. Y. Wang, X. Di, X. Wu, X. Li, MOF-derived nanoporous carbon/ $\text{Co}/\text{Co}_3\text{O}_4/\text{CNTs}/\text{RGO}$ composite with hierarchical structure as a high-efficiency electromagnetic wave absorber. *J. Alloy. Compd.* **846**, 156215 (2020). <https://doi.org/10.1016/j.jallcom.2020.156215>
62. X. Di, Y. Wang, Y. Fu, X. Wu, P. Wang, Wheat flour-derived nanoporous carbon/ ZnFe_2O_4 hierarchical composite as an outstanding microwave absorber. *Carbon* **173**, 174–184 (2021). <https://doi.org/10.1016/j.carbon.2020.11.006>
63. X. Liu, Y. Huang, L. Ding, X. Zhao, P. Liu et al., Synthesis of covalently bonded reduced graphene oxide- Fe_3O_4 nanocomposites for efficient electromagnetic wave absorption. *J. Mater. Sci. Technol.* **72**, 93–103 (2021). <https://doi.org/10.1016/j.jmst.2020.09.012>
64. Y. Song, F.X. Yin, C.W. Zhang, W.B. Guo, L.Y. Han et al., Three-dimensional ordered mesoporous carbon spheres modified with ultrafine zinc oxide nanoparticles for enhanced microwave absorption properties. *Nano-Micro Lett.* **13**, 76 (2021). <https://doi.org/10.1007/s40820-021-00601-x>
65. C. Zhang, Y. Peng, Y. Song, J. Li, F. Yin et al., Periodic three-dimensional nitrogen-doped mesoporous carbon spheres embedded with $\text{Co}/\text{Co}_3\text{O}_4$ nanoparticles toward microwave absorption. *ACS Appl. Mater. Interfaces* **12**(21), 24102–24111 (2020). <https://doi.org/10.1021/acsami.0c03105>

